

Size, angular momentum and mass for objects

Pablo Anglada, M.E. Gabach-Clement*, Omar E. Ortiz
Facultad de Matemática, Astronomía y Física,
Universidad Nacional de Córdoba,
Instituto de Física Enrique Gaviola, IFEG, CONICET,
Ciudad Universitaria (5000) Córdoba, Argentina.

September 1, 2021

Abstract

We obtain a geometrical inequality involving the ADM mass, the angular momentum and the size of an ordinary, axially symmetric object. We use the monotonicity of the Geroch quasi-local energy on 2-surfaces along the inverse mean curvature flow. We also compute numerical examples to test the robustness of our hypotheses and results

1 Introduction

During the last decade, geometrical inequalities for black holes have received much attention and different relations involving the total mass, the angular momentum, the horizon area, the electromagnetic charge, the cosmological constant and certain shape parameters have been found [9, 17, 1, 12, 7, 30, 8]. The question of whether the same kind of relations hold for ordinary objects (*i.e.* not black holes) is not trivial. Black holes are very special solutions of Einstein equations that can be described by few parameters, at least in the stationary limit. The geometrical inequalities mentioned above show that this no-hair property of the stationary state sets restrictions on the values that physical quantities can have in the general, dynamical black hole state.

On the other hand, ordinary objects like neutron stars are not simple, and hence finding such simple relations is not *a priori* expected. One of the first works in this direction is due to Schoen and Yau [31] (see the discussion and references in [29]). They found a lower bound to the Ricci scalar (and hence, to the matter density) in asymptotically flat initial data only in terms of a certain radius characterizing the object. This in turn gave rise to a black hole formation criteria due to concentration of matter. There were other results similar in nature to this one, namely, quasi-local inequalities between size and matter/currents density for objects, with alternative measures of size [27] [14]. More recently, the Schoen-Yau bound was used by Dain [10] and Khuri [23] under different conditions in axial symmetry, to find a quasi-local relation between angular momentum and size, of the form $J \lesssim \mathcal{R}^2$. Furthermore Khuri [24] also

*gabach@famaf.unc.edu.ar

used it to prove an inequality for charged objects using a similar measure of size. Independently, Reiris [29] derived quasi-local inequalities relating the angular momentum and charge to precise measures of size and shape of ordinary objects. Using a similar approach, Khuri [22] also established inequalities relating size, local mass, angular momentum, and charge, that give rise to black hole existence criteria.

The appropriate measure of the size of an object is not easy to determine, nor is finding its relation with relevant physical quantities, hence these inequalities are not expected to be sharp. Moreover, it is expected that these inequalities become saturated for very special cases, for example the inequality between charge and size, $2\mathcal{R} > Q$, is sharp in the spherically symmetric case with \mathcal{R} the areal radius of the object [3], and the equality is achieved for a sequence of objects whose charge, mass, and radius tend to zero.

Our interest in this article is to relate the rotation of an ordinary object (i.e. its angular momentum) with the total energy (the ADM mass, see [4]) in axially symmetric systems. This approach is inspired by the slow rotation treatment of neutron stars. As discussed in [15], rotating neutron stars are axially symmetric and for slow rotation, the rotational perturbations of the stellar structure are quadratic in the angular velocity and therefore, quadratic in the angular momentum. In the Newtonian limit, one may write the total energy of the star as the sum of two terms, the first including the gravitational and internal energies, denoted as E_0 , and the second, the rotational energy

$$E \approx E_0 + \frac{J^2}{2I} \quad (1)$$

where J is the angular momentum and I the stellar moment of inertia. In 1967 Hartle [16] devised a perturbative method to compute the first order correction to the neutron star's energy in the context of general relativity, and found an expression similar to (1), where the term E_0 represents the total energy for the non-rotating star, and the quadratic term in the angular momentum is the rotational contribution to first order. An extensive study of this equation and different relations between the kinetic and binding energies has been performed since the late 1960's (see [33] for further details and references). It is not our aim to address these problems, but to seek geometrical relations between certain physical parameters for a rotating ordinary object, like the neutron star mentioned above.

Within Newtonian theory, there are no restrictions to the values that the quantities in (1) can attain (we are not considering mechanical processes related to the particular equations of state of matter). Nevertheless, in general relativity, the Hoop conjecture [32] sets bounds on the (quasi-local) mass that an object can have. This conjecture roughly says that if one is able to pass a hoop of radius \mathcal{R} in every direction around a region Ω with (quasi-local) mass m_Ω , then it will collapse to form a black hole if

$$m_\Omega > \frac{\mathcal{R}}{2}. \quad (2)$$

Otherwise, if (2) is not satisfied, one expects an ordinary object.

To incorporate this expected constraint into (1), we start with the Newtonian

definition of moment of inertia of Ω with respect to the symmetry axis

$$I := \int_{\Omega} \mu \rho^2 dV \quad (3)$$

where μ is the matter density and ρ is the (euclidean) distance from the axis. Moreover, we can roughly write

$$I \approx m_{\Omega} \mathcal{R}_C^2 \quad (4)$$

where m_{Ω} is some measure of the (quasi local) mass contained in the object and $\mathcal{R}_C = \max \rho$ is the circumferential radius. For instance, for a spheroid rotating around the axis of (semi-)length \mathcal{R}_C , the moment of inertia is $2/5 m_{\Omega} \mathcal{R}_C^2$. Then, putting together (2) and (4) we may estimate the following bound to the total energy of a *non-collapsing* object

$$E \gtrsim E_0 + \frac{J^2}{\mathcal{R} \mathcal{R}_C^2}. \quad (5)$$

Although naive and informal, this expression gives a lower bound on the total energy for a rotating system in terms of the angular momentum and two measures of size, that we call \mathcal{R} and \mathcal{R}_C . It is interesting to note that these two quantities come from different contexts. The *distance* to the rotation axis at which matter is located, represented in our argument by the circumferential radius \mathcal{R}_C , seems to be (at least from Newtonian experience) the relevant quantity to describe the kinetic rotational energy. In other words, for rotation it is important to account for the spread out of matter with respect to the symmetry/rotation axis. On the other hand, the measure \mathcal{R} coming from the Hoop conjecture should describe all directions in which matter is spread out. This quantity cares about how localized in every direction matter is.

In this article we present a relation similar to (5) for an ordinary, isolated, rotating and axially symmetric object in general relativity.

The main tools we use to accomplish this are the inverse mean curvature flow (IMCF) and the Geroch energy, which have proven to be useful in obtaining geometrical inequalities in general relativity like the Riemannian Penrose inequality [19]. More related to our system, Dain used the IMCF and the Hawking energy to obtain an inequality between size, ADM mass and electric charge for ordinary objects [11]. Our aim in this article is to explore what the IMCF can say about rotating ordinary objects. The main difficulty being the explicit inclusion of the angular momentum into the geometrical relations.

The article is organized as follows: In section 2 we review the inverse mean curvature flow and some important properties we will use in deriving our result. Also we introduce the Geroch energy and discuss the monotonicity properties. In section 3 we present our hypotheses, the main theorem and discussions. In section 4 we show numerical solutions of the flow equations where we test both some of the hypotheses of our main result, and the geometrical inequality we have found for objects.

2 IMCF and Geroch energy

In this section we review the basic properties of the inverse mean curvature flow (IMCF) and the Geroch energy [20], [34].

Consider a smooth Riemannian 3-manifold M with metric \bar{g}_{ij} , connection $\bar{\nabla}_i$ and Ricci curvature \bar{R}_{ij} . A solution of the IMCF is a smooth family of hypersurfaces $S_t := x(S, t)$ with $x : S \times [0, \tau] \rightarrow M$ satisfying the evolution equation

$$\frac{\partial x}{\partial t} = \frac{\nu}{H} \quad (6)$$

where $t \in [0, \tau]$, $H > 0$ is the mean curvature of the 2-surface S_t at x and ν is the outward unit normal to S_t .

Let g_{ij} be the induced metric on S_t , ∇_i the covariant derivative, h_{ij} the second fundamental form and ds the area element of S_t . Then one can derive the evolution equations (see [20] more details)

$$\frac{\partial}{\partial t} g_{ij} = \frac{2}{H} h_{ij} \quad (7)$$

$$\frac{\partial}{\partial t} (ds) = ds \quad (8)$$

$$\frac{\partial}{\partial t} H = -\Delta(H^{-1}) - H^{-1}(|h|^2 + \bar{R}_{ij}\nu^i\nu^j). \quad (9)$$

It is important to note that when considering the IMCF in axially symmetric initial data, the IMCF equation (6) preserves axial symmetry. That is, if one starts the flow out of a point on the symmetry axis (or out of an axially symmetric initial surface) there is no mechanism that could make the normal to each subsequent surface to have a component along the axial Killing vector. Due to this observation, from now on, when we discuss the IMCF flow, we always consider it consisting of axially symmetric surfaces S_t .

On each surface S_t we introduce the Geroch energy

$$E_G(S_t) := \frac{A_t^{1/2}}{(16\pi)^{3/2}} \left(16\pi - \int_{S_t} H^2 ds \right) \quad (10)$$

where A_t is the area of S_t . This functional has some interesting properties that will be used later in the proof of our result. Namely, for a complete, maximal, asymptotically flat initial data, with non-negative scalar curvature, and surfaces S_t that are topological spheres converging to round spheres at infinity, E_G satisfies

$$E_G(S_t) \geq 0, \quad \frac{dE_G}{dt}(S_t) \geq 0, \quad \lim_{t \rightarrow \infty} E_G(S_t) = m_{ADM}. \quad (11)$$

We refer the reader to [19] for details, proofs and further references. However, since it will be relevant in proving our main theorem, we will sketch the proof of the monotonicity property.

We start with the time derivative of $E_G(S_t)$

$$\begin{aligned} \frac{d}{dt} E_G = \frac{A_t^{1/2}}{(16\pi)^{3/2}} & \left[8\pi - \frac{1}{2} \int_{S_t} H^2 ds + \right. \\ & \left. \int_{S_t} (-H^2 + 2H\Delta(H^{-1}) + 2|h|^2 + 2\bar{R}_{ij}\nu^i\nu^j) ds \right] \quad (12) \end{aligned}$$

where we have used (8) and (9). Then we use the Gauss equation

$$2\bar{R}_{ij}\nu^i\nu^j = \bar{R} + H^2 - |h|^2 - 2\kappa \quad (13)$$

where κ is the Gauss curvature, and obtain

$$\frac{d}{dt}E_G = \frac{A_t^{1/2}}{(16\pi)^{3/2}} \left[8\pi + \int_{S_t} \left(2H\Delta(H^{-1}) + |h|^2 + \bar{R} - 2\kappa - \frac{H^2}{2} \right) ds \right]. \quad (14)$$

Rewriting the $|h|^2$ term in terms of the principal curvatures λ_1 and λ_2 and the mean curvature we find

$$\frac{d}{dt}E_G = \frac{A_t^{1/2}}{(16\pi)^{3/2}} \left[8\pi + \int_{S_t} \left(2H\Delta(H^{-1}) + \frac{1}{2}(\lambda_1 - \lambda_2)^2 + \bar{R} - 2\kappa \right) ds \right]. \quad (15)$$

Next, we use the Gauss-Bonnet theorem and integrate by parts the Laplace operator

$$\frac{d}{dt}E_G = \frac{A_t^{1/2}}{(16\pi)^{3/2}} \left[8\pi - 4\pi\chi(S_t) + \int_{S_t} \left(2\frac{|\nabla H|^2}{H^2} + \frac{1}{2}(\lambda_1 - \lambda_2)^2 + \bar{R} \right) ds \right] \quad (16)$$

where $\chi(S_t)$ is the surface's Euler characteristic. If the surfaces S_t are topological spheres we have

$$\frac{d}{dt}E_G = \frac{A_t^{1/2}}{(16\pi)^{3/2}} \int_{S_t} \left(2\frac{|\nabla H|^2}{H^2} + \frac{1}{2}(\lambda_1 - \lambda_2)^2 + \bar{R} \right) ds \quad (17)$$

from where we see that if the 3-manifold has nonnegative scalar curvature, then the Geroch energy is non-decreasing, that is $dE_G/dt \geq 0$.

3 Main result

Following [26], we consider a complete initial data $(M, \bar{g}, K; \mu, j)$, where K is the extrinsic curvature of the 3-manifold M , and μ, j are the matter density and the matter current density respectively. We take this initial data to be maximal, asymptotically flat and axially symmetric, and we assume it satisfies the Dominant Energy Condition (DEC), $\mu \geq |j|$. Since we are concerned with ordinary objects, as opposed to black holes, we also require the initial data to have no minimal surfaces. The definition of a rotating object we will use is the following:

Definition 3.1. *Object: Open set Ω in M which is axially symmetric, compact, connected and such that the matter current density j has compact support in Ω .*

Assume that on (M, \bar{g}) there exists a smooth inverse mean curvature flow of compact surfaces S_t , having spherical topology and going to round spheres at infinity. Our aim is to relate the region Ω with the surfaces given by the IMCF to obtain a geometrical inequality involving physical parameters of Ω . In order to do this, we will take into account the fact that the asymptotic behavior of the surfaces S_t implies that after some time T , S_t will be convex. And also, the fact that maximality of the initial data, together with the DEC imply, via

the constraint equations, that $\bar{R} \geq 0$, and hence the Geroch energy is non-decreasing. This will be crucial in what follows. It is also important to note that the assumption about the smoothness of the flow could be relaxed. That is, some parts of our derivation do not require smoothness, and can be done using the weak level set version of the flow defined by Huisken and Ilmanen [19]. Nevertheless, for simplicity of presentation we consider only the smooth case in this article.

Besides the ADM mass, m_{ADM} , the physical and geometrical quantities we are interested in are the Komar angular momentum $J(S)$ and the areal and circumferential radii of a surface S in M :

$$J(S) = \frac{1}{8\pi} \int_S K_{ij} \eta^i \nu^j ds, \quad (18)$$

$$\mathcal{R}_A(S) := \sqrt{\frac{A}{4\pi}}, \quad \mathcal{R}_C(S) := \frac{C}{2\pi} \quad (19)$$

where η^i is the Killing vector field associated to the axial symmetry, A is the area of S and C is the length of the greatest axisymmetric circle of S .

We find the following result.

Theorem 3.2. *Let $(M, \bar{g}, K; \mu, j)$ be a maximal, asymptotically flat, axially symmetric initial data, that contains an object Ω ; the data satisfies the dominant energy condition and has no minimal surfaces. Assume there exists a smooth IMCF of surfaces S_t on M starting from a point on the symmetry axis inside Ω and such that S_t is convex for $t \geq T \in \mathbb{R}$ and S_T encloses the object. Then*

$$m_{ADM} \geq m_T + \frac{1}{5} \frac{J^2}{\mathcal{R}_A \mathcal{R}_C^2} \quad (20)$$

where J , \mathcal{R}_A and \mathcal{R}_C are the angular momentum, areal radius and circumferential radius of S_T respectively, and

$$m_T := \frac{1}{16\pi} \int_0^{\mathcal{R}_A} d\xi \int_{S_\xi} \bar{R} ds \quad (21)$$

and ξ stands for the areal radius coordinate.

Proof. The scheme of the proof is to start with the time derivative of the Geroch energy (17), bound away the $|\nabla H|^2$ and $(\lambda_1 - \lambda_2)^2$ terms and use the constraint equations to write \bar{R} in terms of the angular momentum. Then integrate in the flow parameter t to infinity.

With this in mind, we have the bound (for simplicity we omit the area element ds when possible)

$$\frac{d}{dt} E_G \geq \frac{A_t^{1/2}}{(16\pi)^{3/2}} \int_{S_t} [16\pi\mu + K_{ij} K^{ij}] \quad (22)$$

where we have used the constraint $\bar{R} = 16\pi\mu + K_{ij} K^{ij} - (\text{tr}K)^2$ and maximality (i.e. $\text{tr}K = 0$). In order to include the angular momentum into the inequality,

we use the Cauchy-Schwarz inequality in the definition of $J_t := J(S_t)$

$$\begin{aligned} J_t^2 &= \left(\frac{1}{8\pi} \left| \int_{S_t} K_{ij} \eta^i \nu^j \right| \right)^2 \leq \frac{1}{(8\pi)^2} \left(\int_{S_t} |K_{ij} \eta^i \nu^j| \right)^2 \\ &\leq \frac{1}{(8\pi)^2} \left(\int_{S_t} |K_{ij}| \sqrt{\eta} \right)^2 \leq \frac{1}{(8\pi)^2} \int_{S_t} |K_{ij}|^2 \int_{S_t} \eta \end{aligned} \quad (23)$$

where $\eta := \eta_i \eta^i$ is the square norm of η^i and in the fourth step we have used the Hölder inequality with $p = q = 2$. Hence, we have a bound for the angular momentum of S_t in terms of the extrinsic curvature (and hence, of the scalar curvature):

$$\int_{S_t} K_{ij} K^{ij} \geq (8\pi)^2 \frac{J_t^2}{\int_{S_t} \eta}. \quad (24)$$

Putting this into (22) we get

$$\frac{d}{dt} E_G \geq \frac{A_t^{1/2}}{(16\pi)^{3/2}} \left[\int_{S_t} 16\pi\mu + (8\pi)^2 \frac{J_t^2}{\int_{S_t} \eta} \right]. \quad (25)$$

Now, let T be the smallest time such that for $t \geq T$ the surfaces given by the flow are convex and such that S_T encloses the object we are interested in.

Assuming there are no minimal surfaces in the space, the flow goes to infinity. We integrate equation (22) from the initial time to T and then to infinity. We first show that the integral of (22) from 0 to T is just the quasi-local mass m_T . We start with the scalar constraint equation $\bar{R} = 16\pi\mu + K_{ij}K^{ij}$ and change the coordinate t to the areal radius coordinate $\xi(t) = \sqrt{\frac{A_t}{4\pi}}$. We have $T \rightarrow \xi(T) = \sqrt{\frac{A_T}{4\pi}} = \mathcal{R}_A$ and $dt \rightarrow d\xi = \sqrt{\frac{A_t}{16\pi}} dt$, thus:

$$\int_0^T \frac{A_t^{1/2}}{(16\pi)^{3/2}} \int_{S_t} \bar{R} ds dt = \frac{1}{16\pi} \int_0^{\mathcal{R}_A} d\xi \int_{S_\xi} \bar{R} ds = m_T \quad (26)$$

Then for the range $[T, \infty)$ we use equation (25) instead of (22) to explicitly include the angular momentum. Due to the compact support of j , J_t is conserved outside S_T . Therefore $J_t = J_T := J$, and hence, disregarding the positive term involving μ and using the relation between the Geroch energy and the ADM mass at infinity, we obtain

$$m_{ADM} \geq \lim_{t \rightarrow \infty} E_G(S_t) \geq m_T + \sqrt{\pi} J^2 \int_T^\infty \frac{A_t^{1/2}}{\int_{S_t} \eta} dt. \quad (27)$$

Next we need to bound the surface integral of η . Here it is where convexity plays a role. We introduce orthogonal coordinates θ, φ for the surface S_t such that $\eta^i = \left(\frac{\partial}{\partial \varphi} \right)^i$. One can always do this for axially symmetric 2-surfaces that are diffeomorphic to S^2 , see for example [12]. Then we write the evolution equation (7) in the form

$$\frac{\partial}{\partial t} \eta = \frac{\partial}{\partial t} g_{\varphi\varphi} = \frac{2}{H} h_{\varphi\varphi}. \quad (28)$$

Recall that in axial symmetry the principal and mean curvatures are given by

$$\lambda_1 = g^{\theta\theta} h_{\theta\theta}, \quad \lambda_2 = g^{\varphi\varphi} h_{\varphi\varphi} \quad (29)$$

$$H = g^{ij} h_{ij} = g^{\theta\theta} h_{\theta\theta} + g^{\varphi\varphi} h_{\varphi\varphi} = \lambda_1 + \lambda_2. \quad (30)$$

Therefore we have

$$h_{\varphi\varphi} = \frac{\lambda_2}{g^{\varphi\varphi}} = g_{\varphi\varphi} \lambda_2 = \eta \lambda_2. \quad (31)$$

Putting this into (28) we find

$$\frac{\partial}{\partial t} \eta = 2\eta \frac{\lambda_2}{H}. \quad (32)$$

Now, we use this equation for $t \geq T$, where the surfaces are strictly convex, and therefore $\lambda_1, \lambda_2 > 0$ and $\lambda_2 \leq H$. This gives us

$$\frac{\partial}{\partial t} \eta \leq 2\eta \quad (33)$$

and

$$\frac{\partial}{\partial t} (\eta dS) = \frac{\partial \eta}{\partial t} dS + \eta dS \leq 2\eta dS + \eta dS = 3\eta dS. \quad (34)$$

Therefore we can write $\eta dS \leq \eta_T e^{3(t-T)} dS_T$ and have

$$\int_{S_t} \eta \leq e^{3(t-T)} \int_{S_T} \eta_T \leq e^{3(t-T)} A_T \max_{S_T} \eta, \quad t \geq T. \quad (35)$$

Also, using $A_t = e^{(t-T)} A_T$ we bound

$$\begin{aligned} m_{ADM} &\geq m_T + \sqrt{\pi} J^2 \int_T^\infty \frac{A_T^{1/2} e^{(t-T)/2}}{e^{3(t-T)} A_T \max_{S_T} \eta} dt \\ &\geq m_T + \frac{2\sqrt{\pi}}{5} \frac{J^2}{A_T^{1/2} \max_{S_T} \eta} \end{aligned} \quad (36)$$

where m_T , given by (26) comes from integrating (22) in the interval $t \in (0, T)$.

Finally we write this expression in terms of the areal and circumferential radii (19) and obtain (20). □

Remarks

The inequality (20) is global in nature as it involves the ADM mass. This is different from the quasi-local inequalities mentioned in the Introduction. We also note that the Geroch energy seems to be a very appropriate quasi-local mass for our purposes. On one hand, it converges to the ADM mass. And on the other hand, it is directly related to the mean curvature of the surface, and therefore, its time derivative along the flow is related to the scalar curvature of the initial data, which we were able to bound in terms of the angular momentum. The natural question is whether one can write a different quasi-local quantity E , having both properties, that is, $E \rightarrow m_{ADM}$ and $E \sim H^2$ and such that it produces a better, sharper inequality.

The inequality (20) is linear in the ADM mass and quadratic in the angular momentum as a result of the linear dependence of dE_G/dt with the scalar curvature \bar{R} . This is to be confronted with the linear relation suggested by the Bekenstein conjecture for the entropy of macroscopic objects [5] [18]. The positivity of the entropy function implies the bound $\mathcal{E} \geq |J|/\mathcal{R}$ where \mathcal{E} is the total energy and \mathcal{R} is the radius of the smallest sphere that encloses the object (note the similar dependence for the case of black holes [13]). However, the quadratic relation seen in (20) is in accordance with the Newtonian limit (5). Indeed, the parallelism is clear if one takes the hoop radius as the areal radius \mathcal{R}_A . An important question is whether this discrepancy between the Bekenstein conjecture and our own result for the relation between mass and angular momentum is due to the hypotheses in our theorem. We do not have a clear answer for that, but we note, as pointed out by Unruh and Wald [35], that the Bekenstein bound is not essential for the validity of the generalized laws of thermodynamics ¹, and might not be optimal.

Disregarding the non-negative m_T term and re-writing inequality (20) in the form

$$\mathcal{R}_C^2 \geq \frac{1}{5} \frac{J^2}{m_{ADM} \mathcal{R}_A} \quad (37)$$

we see that if we fix the total mass and the area of the object, then the greater the angular momentum, the greater the circumferential radius. This result agrees with our expectation and experience that rotation produces flattening. We see that rotation sets restrictions onto how prolate an ordinary object can be. Also, this inequality gives information about localization in space. It implies that for given total energy m_{ADM} , a rotating region can not be too small. Note that there is an important difference between this kind of argument and the ones used in black hole formation criteria, where only quasi-local quantities are taken into account. We will come back to this issue below.

No equations of state were assumed. Inequality (20) is a consequence of Einstein constraint equations and does not occur in pure Newtonian theory (recall that in the introduction we obtained a similar inequality (5) after assuming the Hoop condition (2)). Matter enters the inequality only via the m_T term and the dominant energy condition needed to make the Geroch energy have the positivity and monotonicity properties.

When Maxwell fields are taken into account, the inequality can be extended using similar techniques, provided that there is no electromagnetic contribution to the angular momentum outside the body. For the treatment of the electromagnetic contributions we follow the work of Dain [11], where the case of time symmetric data with no rotation, $J = 0$, was considered.

We write the energy density in the form

$$\mu = \mu_{(\text{not EM})} + \frac{E^2 + B^2}{8\pi} \quad (38)$$

where $\mu_{(\text{not EM})}$ stands for non-electromagnetic matter fields satisfying the dominant energy condition, and E^i , B^i are the electromagnetic fields. Then

¹We thank an anonymous referee for making this observation to us.

the integral in (22) has three terms, the ones involving $\mu_{(\text{not EM})}$ and $K_{ij}K^{ij}$ are treated in exactly the same manner as before. The term involving the electromagnetic contribution to the energy density could be bound in terms of the electric charge by following [21]. We sketch the proof below.

$$\begin{aligned} \frac{A_t^{1/2}}{(16\pi)^{1/2}} \int_{S_t} \mu &= \frac{A_t^{1/2}}{(16\pi)^{3/2}} \int_{S_t} 2(E^2 + B^2) \geq \frac{2A_t^{1/2}}{(16\pi)^{3/2}} \int_{S_t} (E^j \nu_j)^2 \\ &\geq \frac{2A_t^{1/2}}{(16\pi)^{3/2}} \frac{\left(\int_{S_t} E^j \nu_j\right)^2}{A_t} \geq \frac{2\left(\int_{S_t} E^j \nu_j\right)^2}{(16\pi)^{3/2} A_t^{1/2}} = \frac{\sqrt{\pi} Q_t^2}{2A_t^{1/2}}. \end{aligned} \quad (39)$$

In the third step we used the Hölder inequality, and in the fifth step we used the Gauss theorem and the definition of electric charge

$$Q_t = \frac{1}{8\pi} \int_{S_t} E^j \nu_j. \quad (40)$$

Let T be the smallest value of the flow parameter such that for $t \geq T$ the surfaces given by the flow are convex and such that it encloses the object (we still need this convexity condition to control the rotation part of the evolution). Then since S_t lays outside the object, the electric charge is $Q_t = Q_T := Q$, and thus for $t > T$ the time derivative of the Geroch energy is bounded by

$$\frac{d}{dt} E_G \geq \frac{\sqrt{\pi} A_t^{1/2}}{\int_{S_t} \eta} J^2 + \frac{\sqrt{\pi}}{2A_t^{1/2}} Q^2. \quad (41)$$

Integrating (22) from 0 to infinity, using (41) and (11), we obtain:

$$m_{ADM} \geq m_T + \frac{1}{2} \frac{Q^2}{\mathcal{R}_A} + \frac{1}{5} \frac{J^2}{\mathcal{R}_A \mathcal{R}_C^2}. \quad (42)$$

where again m_T , given by (26), comes from integrating (22) in the interval $t \in (0, T)$. Note that the electric part of this inequality does not depend on the circumferential radius, only the size (measured by the surface area) is relevant in that case.

The final remark we want to make is about where we start the IMCF. In our theorem and treatment so far, we started out from a point on the symmetry axis in M and cover all M with the surfaces S_t . In particular, we look at one of these surfaces, that we call S_T , to obtain information about the object's physical and geometrical properties. However that might not be the most convenient way of studying the object, as one might lose control over where S_T is or how far away from the object it is. We know from Huisken and Ilmanen's work [19] that for sufficiently large times, the surfaces are convex (as they approach round spheres at infinity), but clearly, one of such surfaces near infinity would not give a good description of the object's size. Unfortunately, one does not *a priori* know where S_T will be located. An alternative approach is to start the flow from a convex surface S_0 , chosen in such a way that its evolution preserves convexity and, more importantly, such that it coincides with the object's surface or it is

the smallest surface enclosing it. By following this procedure we arrive at the following inequality

$$m_{ADM} \geq E_G(S_0) + \frac{1}{5} \frac{J^2}{\mathcal{R}_A \mathcal{R}_C^2} \quad (43)$$

where now $E_G(S_0)$ is the Geroch energy of the initial surface S_0 and the quantities J , \mathcal{R}_A , \mathcal{R}_C refer to S_0 as well. This approach is particularly useful for numerical calculations and it is the one we use in the next section.

There are important open questions we want to address next. The first one being the convexity condition, we present some ideas and numerical results in the next section. Secondly is the appropriate notion of size one should use. In axial symmetry, the areal and circumferential radii are well defined and are related to relevant properties of the region under study, that is, localization and rotation. However, extending these ideas outside axial symmetry does not seem straightforward and a more general measure of size should be introduced. Another issue has to do with the boundary between ordinary objects (like the ones we study here) and black holes. More precisely, could we use this inequality to formulate a black hole formation criteria similar to the one proved by Khuri [23]? We see that there are differences between our work and that of Khuri, because we include a global quantity, the ADM mass. Therefore, our inequality does not lend itself directly to an argument of the kind 'if the angular momentum is too localized, then a black hole will form'. In our main result, the localization of angular momentum, represented by the ratio $(angular\ momentum)(size)^{-1}$ is compared to the total energy. Finally, we would like to understand better the relation between our approach to study inequalities for ordinary objects and the arguments involved in the derivation of the Penrose inequality [2].

4 Numerical tests

An important ingredient in our result is the convexity of surfaces S_t along the IMCF evolution. In this section we want to show that, in particular examples, this property of the flow holds even when the surfaces S_t are close to the object. Also, we want to evaluate the relative importance of the term involving the angular momentum in our inequalities. For these purposes we want to compute the IMCF starting with an initial surface which is good to represent the physical and geometrical properties of the object, and therefore we study the inequality in the form (43) to choose an initial surface S_0 that is *as close as possible* to $\partial\Omega$.

We expect that within our approach, the convexity of the flow could be relaxed. This is suggested by the convergence properties of the last integral in (27). This point will be studied in detail [2].

Every numerical example in this section is computed in two stages. First, the elliptic problem for the conformal factor Ψ is solved, giving an initial data set. This initial data set is completely determined by a compact material object with maximum angular momentum J compatible with the dominant energy condition (see Appendix A). Secondly, the IMCF equation is used to compute the evolution of a convex initial surface S_0 that tightly encloses the object. The

preservation of the surface's convexity along the flow and our main inequality are then checked.

4.1 Computation of the conformal factor Ψ

We restrict our numerical examples to initial data sets which are maximal, asymptotically flat, and conformally flat. The exact set up and assumptions, and the derivation of the equations involved are described in the Appendix A.

Let (ρ, φ, z) be cylindrical coordinates on the conformal, flat geometry, adapted to the axial symmetry of our problem, where we need to solve the equation for Ψ . Because of the axial symmetry, no function depends on φ . The conformal factor Ψ , and thus the initial data set defined on the initial slice $M = \mathbb{R}^3$, is the solution of the semi-linear elliptic problem (83),(87), deduced in the Appendix A. In cylindrical coordinates, this problem is

$$\begin{aligned} \Delta \Psi &= -\frac{2\pi a \rho}{\Psi^3} - \frac{|\partial f|^2 \rho^2}{4\Psi^7}, \\ \partial_\rho \Psi(\rho=0) &= 0, \quad \lim_{r \rightarrow \infty} \Psi(\rho, z) = 1, \quad r = \sqrt{\rho^2 + z^2}, \end{aligned} \quad (44)$$

where Δ is the flat Laplacian and the function $f(\rho, z)$ is, in turn, a solution of the linear elliptic problem

$$\begin{aligned} \partial_\rho^2 f + \partial_z^2 f + \frac{3\partial_\rho f}{\rho} &= -8\pi a, \\ \partial_\rho f(\rho=0) &= 0, \quad \lim_{r \rightarrow \infty} f(\rho, z) = 0, \quad r = \sqrt{\rho^2 + z^2}. \end{aligned} \quad (45)$$

The positive function $a(\rho, z)$ appearing in the source of both equations is a free function that determines the matter content and the angular momentum content of the initial data. In our examples we choose this function to have compact support.

The angular momentum content, equation (89), in any region Ω of the initial slice is given by

$$J = - \int_{\Omega} a \rho^2 dv_0. \quad (46)$$

Here and in what follows, dv_0 denotes the volume element on the flat, conformal geometry. Once Ψ is computed, by solving the problem (44),(45), the rest of the physically relevant quantities (see Appendix B) can be computed. The area of an axisymmetric surface $\partial\Omega$ is given by equation (91), from which areal radius \mathcal{R}_A is obtained. The circumferential radius $\mathcal{R}_C = \mathcal{C}/2\pi$, is computed by finding the greatest axisymmetric circle \mathcal{C} of $\partial\Omega$. The average baryonic mass density of the object is $\rho_b = M_b/V$ with the baryonic mass and volume of the object given by

$$M_b = \int_{\Omega} \frac{\rho a}{\Psi^2} dv_0, \quad \text{and} \quad V = \int_{\Omega} \Psi^6 dv_0. \quad (47)$$

Here Ω is the support of the function a .

The ADM mass of the initial data can be computed as a volume integral on the whole space (equation (88)).

To solve the problem (44),(45), we proceed as follows. First, in all our examples we choose, for simplicity, matter content (function a) to satisfy reflection

symmetry on the plane $z = 0$, i.e., $a(\rho, -z) = a(\rho, z)$. This property effectively reduces the problem to half size; one needs to solve only for $z \geq 0$. Regularity of the solution at $z = 0$ becomes homogeneous Neuman boundary condition at $z = 0$. Second, we compactify the problem by introducing new coordinates so that the whole quarter ρ - z plane maps to a unit square. The new coordinates are

$$x = \frac{\rho}{\rho + \rho_H}, \quad y = \frac{z}{z + z_H}, \quad (48)$$

where the parameters $\rho_H > 0$ and $z_H > 0$ can be freely chosen. The symmetry axis, $\rho = 0$ maps to $x = 0$, $\rho = \infty$ maps to $x = 1$ and $\rho = \rho_H$ maps to $x = 1/2$. Analogously, the plane $z = 0$ maps to $y = 0$, $z = \infty$ maps to $y = 1$, and $z = z_H$ maps to $y = 1/2$. Summarizing, the compact elliptic problem we need to solve, in the square $0 \leq x, y \leq 1$, is

$$\frac{(1-x)^4}{\rho_H^2} f_{xx} + \frac{(1-x)^3(3-2x)}{x\rho_H^2} f_x + \frac{(1-y)^4}{z_H^2} f_{yy} - 2\frac{(1-y)^3}{z_H^2} f_y = -8\pi a, \quad (49)$$

with boundary conditions

$$f_x(0, y) = f_y(x, 0) = 0, \quad f(1, y) = f(x, 1) = 0, \quad (50)$$

and

$$\begin{aligned} \frac{(1-x)^4}{\rho_H^2} \Psi_{xx} + \frac{(1-x)^3(1-2x)}{x\rho_H^2} \Psi_x + \frac{(1-y)^4}{z_H^2} \Psi_{yy} - 2\frac{(1-y)^3}{z_H^2} \Psi_y \\ = -2\pi\rho_H \frac{x a}{(1-x)\Psi^3} - \frac{\rho_H^2}{4} \frac{x^2 |\partial f|}{(1-x)^2 \Psi^7}, \end{aligned} \quad (51)$$

with boundary conditions

$$\Psi_x(0, y) = \Psi_y(x, 0) = 0, \quad \Psi(1, y) = \Psi(x, 1) = 1. \quad (52)$$

To compute the solution to these problems we use finite differences. We discretize x and y in uniform grids

$$x_i = hi, \quad y_j = hj, \quad i, j = -2, -1, 0, 1, 2, \dots, N-1, N, \quad (53)$$

where the mesh size is $h = 1/N$, and we choose $N = 2^k$, being k a positive integer. The index values from 0 to N cover the unit square including the boundaries, while the ghost values $-2, -1$ are used to impose the homogeneous Neuman boundary conditions.

All functions of the problem become grid-functions. To discretize the equations we use standard difference operators which are fourth order accurate all over the domain, centered in the interior of the domain, and semilateral and lateral close to and on the outer border of the domain.

Let us denote $v_{i,j} = v(x_i, y_j)$ the solution of any of the equations (49) or (51). The values $v_{N,j}$, $j = 0, 1, \dots, N$ and $v_{i,N}$, $i = 0, 1, \dots, N$ are fixed by the Dirichlet boundary condition at infinity. The homogeneous Neuman boundary conditions at $x = 0$ and $y = 0$ are imposed by setting the ghost points $i = -2, -1$ and $j = -2, -1$ in the way

$$\begin{aligned} v_{-2,j} = v_{2,j}, \quad v_{-1,j} = v_{1,j}, \quad j = 0, 1, \dots, N, \\ v_{i,-2} = v_{i,2}, \quad v_{i,-1} = v_{i,1}, \quad i = 0, 1, \dots, N. \end{aligned} \quad (54)$$

The algebraic linear system of equations obtained for $f_{i,j}$ could be solved by a direct method (like LU -decomposition plus Gaussian elimination). The algebraic, non-linear system of equations obtained for $\Psi_{i,j}$, however, has to be solved by an iterative method. For simplicity we decided to use iterative methods to solve both equations.

To accelerate convergence, we use a multigrid algorithm [6]. In all cases we use under relaxed Jacobi smothers on the finest and intermediate grids, and over relaxed Jacobi on the coarsest grid. The number of grid levels one can use in these problems, having in mind the span of the difference operators, is upper bounded by $k - 3$. The grid functions are passed from a fine grid to the next coarser grid by simple restriction. The prolongation of a grid function from a coarse grid to a finer grid is carried out by cubic Hermite interpolation.

The initial iteration has to be chosen carefully in these iterative schemes, so that the overall method converges. In some cases it is enough to choose $f_{i,j} = 0$ and $\Psi_{i,j} = 1$, but sometimes, on fine grids, it is necessary to start with an interpolated coarser-grid solution.

In our code the multigrid algorithm is applied as a sequence of V -cycles[6]. After a number of V -cycles, the maximum norms of the residual and the increment of the solution $\delta v_{i,j}$ on the finest grid are checked. If the relative values of these two norms, with respect of the norm of the solution itself, are smaller than $\epsilon = 10^{-10}$, the iterations are stopped. In the equation for $\Psi_{i,j}$, the non linearity is treated with the full approximation storage (FAS) algorithm[6]. For every example presented in this paper, we compute the conformal factor Ψ on three grids with $N = 128$, $N = 256$ and $N = 512$, and use the three solutions to check convergence of the difference scheme.

All the integrals used to compute physically relevant quantities are approximated by the Simpson's rule.

4.2 Numerical setup for the IMCF equation

We want to solve numerically the ordinary problem given by (99)-(100), starting with an initial surface at $t = 0$ that is convex and that just encloses the object under study. This problem, though differentially ordinary, is tricky to be solved numerically. This is so because its exact solutions diverge exponentially with time. The problem is therefore unstable; one has to be careful when choosing a numerical scheme to approximate its solution, since any perturbation (deviation from the exact solution) will also grow exponentially with time. What we need is a conditionally stable scheme, which basically means that the numerically computed approximation does not diverge faster than the exact solution[25].

We discretize the variable θ on a uniform grid and approximate the derivatives with respect to θ by standard, centered, fourth order accurate finite difference operators. The regularity of $v(\theta, t)$ at $\theta = 0$ and the regularity plus reflection symmetry in the $z = 0$ plane imply Neuman boundary conditions at $\theta = 0$ and $\theta = \pi/2$. These boundary conditions are well handled (imposed) by using two ghost points on each side of the interval $[0, \pi/2]$.

To integrate in time, one can choose a fourth order accurate method too. However, this is not worth the price. The reason is that the eigenvalues of the linearized equation are positive and large and then, to have a conditionally stable scheme, the time step has to be very small as compared with the mesh size and a low order method can do the job. The explicit Euler method turned out to be

appropriate for our problem because the overall method (fourth order in space and first order in time) becomes conditionally stable for the discretizations we use when the time step is comparable to the fourth power of the mesh size. If the time step is not small enough, regardless of the time integration method, the method becomes unstable and the solution breaks with peaks that diverge in a few time steps. In our calculations we use a mesh size $\delta_\theta = \pi/200$ and time steps as small 2×10^{-6} .

4.3 Object models and results

In our setup an initial data is completely defined by the function $a(\rho, z)$. The finite difference approximations described in the previous section have truncation errors that involve, in the leading term, fifth and sixth order derivatives of the solution. Therefore, to not ruin the accuracy of the computed approximation and the convergence rate of the iterative methods, the function a defining the object has to be at least C^4 -smooth on the computational domain. So, we study objects given by compactly supported functions $a(\rho, z)$ which are defined in terms of the cutoff polynomial $q(s)$ given by

$$q(s) = 1 - s^4 \left(1 - 5(s-1) + 15(s-1)^2 - 35(s-1)^3 + 70(s-1)^4 \right). \quad (55)$$

All the magnitudes given in this section are in geometrical units in the cgs system.

4.3.1 Spheroidal objects

For these examples we choose the function a to have support on an axially symmetric ellipsoid, which can be either oblate or prolate (being a sphere a particular case),

$$a(\rho, z) = \begin{cases} a_0 q(s), & 0 \leq s < 1, \\ 0, & 1 \leq s, \end{cases} \quad (56)$$

where

$$s = \sqrt{\left(\frac{\rho}{R}\right)^2 + \left(\frac{z}{Z}\right)^2}$$

and R, Z are positive constant. The functions $a(\rho, z)$ so defined are C^4 -smooth on the whole domain. The support region Ω is given by $s < 1$, while the surface of the object, $\partial\Omega$, is given by $s = 1$.

In Table 1 we present various spheroidal objects of different densities and sizes. The parameters a_0 , R and Z are displayed together with the resulting angular momentum J . The object called NS is chosen to be slightly oblate, and has parameters so that the baryonic mass density and object size are comparable to those of a neutron star (see Table 2 and, for example, [28]). The following three objects, P , O and VO , have the same value of a_0 and similar size parameters, which result in comparable baryonic densities. P is a prolate spheroid; O an oblate spheroid and VO a very oblate spheroid. The object called S is a larger and lighter, slightly prolate, spheroid with parameters chosen so that the resulting size and baryonic mass density are comparable to those of the sun.

In Table 2 we show, for each object in Table 1, the average baryonic density of the object, the physical size of the object represented by the radii \mathcal{R}_A and

Obj.	a_0	R	Z	J
NS	6.00×10^{-18}	7.50×10^5	7.30×10^5	1.4614×10^{11}
P	6.00×10^{-18}	0.80×10^6	1.00×10^6	2.5916×10^{11}
O	6.00×10^{-18}	1.00×10^6	0.80×10^6	5.0617×10^{11}
VO	6.00×10^{-18}	1.00×10^6	0.30×10^6	1.8981×10^{11}
S	2.90×10^{-38}	6.70×10^{10}	6.5×10^{10}	4.0056×10^{15}

Table 1: Parameters defining various spheroidal objects.

Obj.	ρ_b	\mathcal{R}_C	\mathcal{R}_A	m_{ADM}	convex?
NS	4.3247×10^{-14}	1.0461×10^6	1.0227×10^6	2.7103×10^5	yes
P	3.1137×10^{-14}	1.2309×10^6	1.2859×10^6	3.9647×10^5	yes
O	2.3503×10^{-14}	1.6462×10^6	1.5379×10^6	5.6641×10^5	yes
VO	5.7604×10^{-14}	1.3199×10^6	1.0826×10^6	2.8427×10^5	no
S	1.1212×10^{-28}	6.7000×10^{10}	6.5796×10^{10}	1.3695×10^5	yes

Table 2: Physical quantities for the objects defined in Table 1.

\mathcal{R}_C of the object's surface and the ADM mass m_{ADM} of the initial data. The last column in the table indicates whether the object's surface turns out to be convex or not.

In Table 3 we show, for each object in Table 1, the parameters for the smallest spheroidal surface that encloses the object and is convex. In the cases where the object's surface $\partial\Omega$ is convex, we take it as the initial surface S_0 . In cases where the object's surface is not convex, we take a surface, also defined as an ellipsoid, with larger R or Z so that the surface is convex. We computed the evolution of these surfaces and found that in all cases the convexity is preserved by the IMCF evolution. As examples of these evolutions we show in Figure 1

Obj.	R	Z	\mathcal{R}_C	\mathcal{R}_A	$J^2/(5\mathcal{R}_A\mathcal{R}_C^2)$
NS	7.50×10^5	7.30×10^5	1.0461×10^6	1.0227×10^6	3.8168×10^3
P	0.80×10^6	1.00×10^6	1.2309×10^6	1.2859×10^6	6.8942×10^3
O	1.00×10^6	0.80×10^6	1.6462×10^6	1.5379×10^6	1.2295×10^4
VO	1.00×10^6	0.30×10^6	1.3199×10^6	1.1497×10^6	3.5984×10^3
S	6.70×10^{10}	6.50×10^{10}	6.7000×10^{10}	6.5796×10^{10}	1.0865×10^{-2}

Table 3: Parameters for the initial surface S_0 that preserves convexity when evolved with the IMCF. The geometrical size parameters \mathcal{R}_C and \mathcal{R}_A that measure the size of the object are given together with the quotient on the right hand side in the inequality (20). This last quantity should be compared with the m_{ADM} given in the Table 2.

plots of the surfaces for various times for the NS and VO cases.

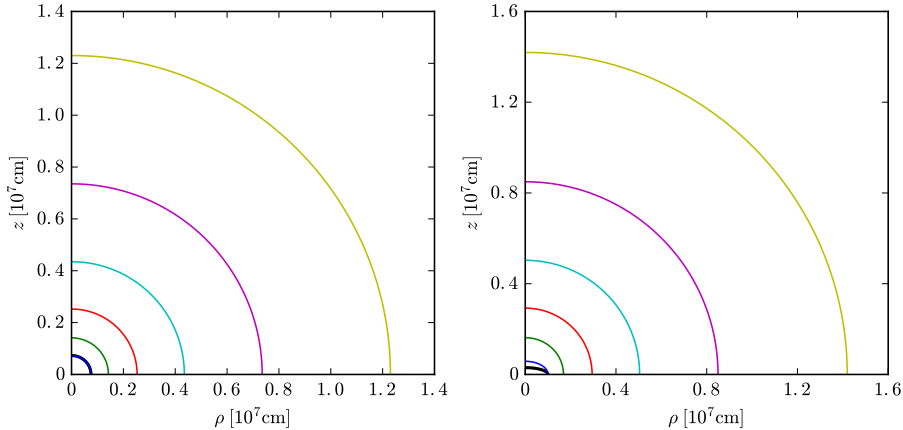


Figure 1: IMCF evolution of the surfaces S_t corresponding to the objects NS (left plot) and VO (right plot) of Table 3. The plots show, from the origin outwards, the surface of the object (thick curve), and the surfaces at times $t = 0, 1.0, 2.0, 3.0, 4.0, 5.0$ in a piece of the ρ - z plane on the flat geometry. In the NS case, the initial surface is coincident with the object's initial surface. In the VO case the initial surface is larger than the object's surface, so chosen so that it is convex.

Figure 2 shows the plot of the principal curvatures (see equations (101) and (102) in Appendix C) of the object's surface for the cases NS and VO. In the first case the positivity of both curvatures show the surface of the body is convex. In the second case the principal curvatures become negative, showing the body surface is not convex.

It is important to check, in all the examples, that the surfaces S_t not only remains convex along the evolution, but also that they approach spheres as time increases. This is clearly seen in plots of the principal curvatures $\lambda_\theta, \lambda_\varphi$. In the Figures 3 and 4 we plot the quotients $\lambda_\theta(\theta)/(1/r(\theta))$ and $\lambda_\varphi(\theta)/(1/r(\theta))$, as functions of θ , for various times, for the two more extreme cases in Table 2: P and VO objects. Both figures show how the principal curvatures of S_t approach the principal curvatures of a sphere as t grows.

4.3.2 Concave object

As a final example we compute the initial data corresponding to an object which is concave even as seen on the conformal flat geometry. We study an object whose function $a(\rho, z)$ is given by equation (56) but in this case the parameter s is defined as

$$s = \frac{\sqrt{\rho^2 + z^2}}{B\left(D + \frac{\rho^2}{\rho^2 + z^2}\right)}. \quad (57)$$

As initial surface S_0 to evolve the IMCF we use a spheroidal surface as before. The object parameters we use in this example are: $B = 5.0 \times 10^5$, $D = 0.3$, $a_0 = 6.0 \times 10^{-18}$. Thus $J = 4.1743 \times 10^{10}$, and we obtain $m_{ADM} = 1.0982 \times 10^5$.

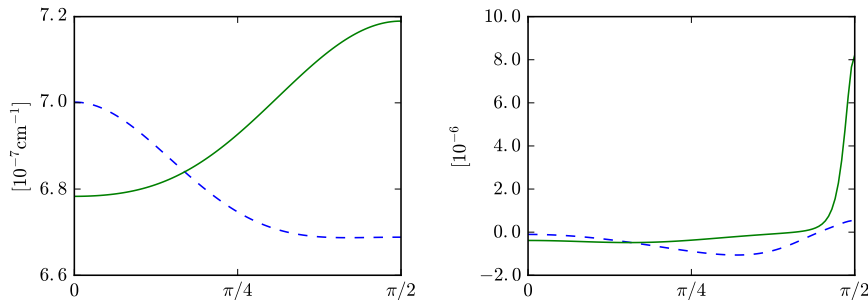


Figure 2: Principal curvatures of the object’s surface for the cases NS (left plot) and VO (right plot) of Table 1. λ_φ is represented in dashed lines and λ_θ in solid lines.

The parameters we use for the convex spheroidal surface S_0 enclosing the body are: $R = 6.60 \times 10^5$, $Z = 3.8 \times 10^5$ and we obtain $\mathcal{R}_A = 6.7350 \times 10^5$ and $\mathcal{R}_C = 7.7969 \times 10^5$. We verify that the IMCF evolution of S_0 preserves convexity and approaches spheres as in the previous cases. A plot of the object surface, initial surface and short time evolution is shown in Figure 5.

4.4 Discussion of numerical results

Our purpose with the numerical examples computed in this section is twofold: first, to check the convexity condition of the surfaces S_t along the IMCF evolution, and second to study the relevance of the $J^2/(5\mathcal{R}_A\mathcal{R}_C^2)$ term on the right hand side in the inequality (43) in various cases. We want to gain insight about when the angular momentum term on the right hand side of the inequality becomes an important contribution as compared with the ADM mass.

The convexity condition of the surfaces along the IMCF evolution is clearly verified in all examples we computed. When the object’s surface is convex, one can evolve the flow starting with $S_0 = \partial\Omega$ (the surface of the object) and the convexity is preserved by the evolution. When the object’s surface is not convex it is enough to choose, it seems, a spheroidal initial surface S_0 that just encloses the object and the evolution preserves the convexity again.

The shape of the objects we consider are simple and our numerical examples far from exhaustive, however we do not find any sign that the IMCF evolution will violate the convexity, at least under the smoothness conditions we impose in our numerical examples. This point certainly deserves a deeper study that we intend to carry out in future works.

To gain insight on the relative importance of the term proportional to J^2 on the right hand side of (43) we define the ratio

$$\Gamma := \frac{\left(\frac{J^2}{5\mathcal{R}_A\mathcal{R}_C^2}\right)}{m_{ADM}}. \quad (58)$$

The values of Γ for the high density objects in Table 1 are

$$\Gamma_{NS} \simeq 1.4 \times 10^{-2}, \quad \Gamma_P \simeq 1.7 \times 10^{-2}, \quad \Gamma_O \simeq 2.2 \times 10^{-2}, \quad \Gamma_{VO} \simeq 1.3 \times 10^{-2},$$

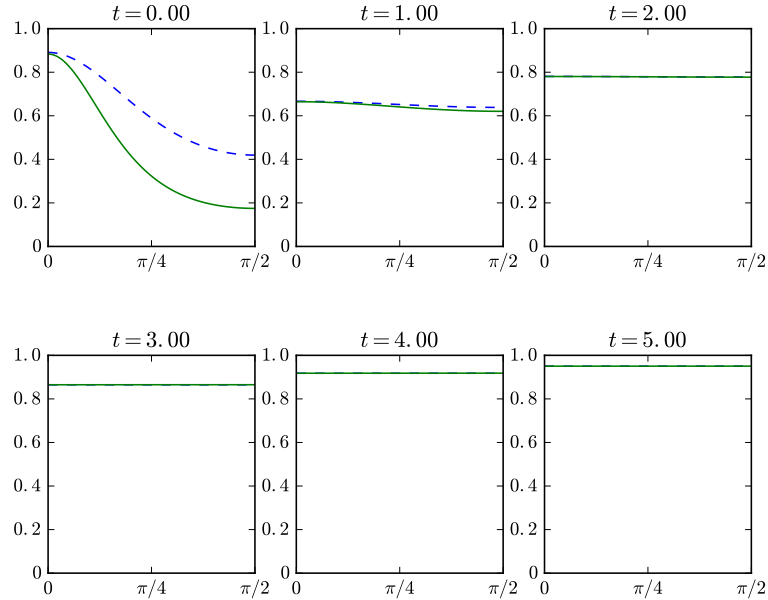


Figure 3: Plots of $r\lambda_\varphi$ (dashed lines) and $r\lambda_\theta$ (solid lines) as functions of θ along the IMCF evolution of the surface of Table 3 for the object P.

while for the lower density object S we have

$$\Gamma_S \simeq 7.9 \times 10^{-8}.$$

For the high density concave object of Section 4.3.2 we get $\Gamma \simeq 7.6 \times 10^{-3}$.

Though we have not computed many examples, our results suggest that the contribution of the J^2 -term is higher for higher density objects. By comparing the values of Γ for the objects P and O , with interchanged values for the parameters R and Z , we see that, as expected, the value of Γ is higher for the oblate spheroid than for the prolate spheroid.

Acknowledgments

P. Anglada and O. E. Ortiz started studying the relationship between size and angular momentum for axially symmetric objects in collaboration with Sergio Dain more than two years ago. All the authors feel deeply indebted to Sergio. M. E. Gabach-Clement wants to thank Marc Mars, Markus Khuri and Greg Galloway for illuminating discussions. This work was supported by grants from CONICET and SECyT, UNC.

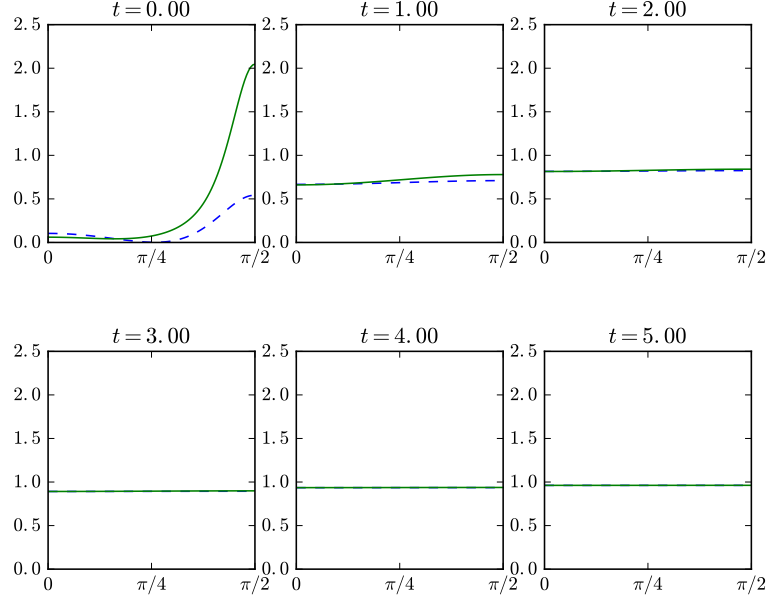


Figure 4: Plots of $r\lambda_\varphi$ (dashed lines) and $r\lambda_\theta$ (solid lines) as functions of θ along the IMCF evolution of the surface of Table 3 for the object VO.

A Conformal method

In this section we derive the constraint equations in the conformally flat case, which is one of the set of equations (together with the flow equations, given in appendix C) we use we use in our numerical computations of section 4.

The conformal method is a well known technique that can be used to simplify the constraints

$$\bar{D}_\beta K^{\alpha\beta} - \bar{D}^\alpha(\text{tr}K) = -8\pi j^\alpha, \quad (59)$$

$$\bar{R} - K_{\alpha\beta}K^{\alpha\beta} + (\text{tr}K)^2 = 16\pi\mu, \quad (60)$$

where \bar{D} and \bar{R} are the Levi-Civita connection and the curvature scalar associated with \bar{g} .

We restrict to the maximal case ($\text{tr}K=0$) and take $\tilde{g}_{\alpha\beta}$, and $\tilde{K}_{\alpha\beta}$ to be symmetric tensor fields such that

$$\bar{g}_{\alpha\beta} = \Psi^4 \tilde{g}_{\alpha\beta} \quad K_{\alpha\beta} = \Psi^{-2} \tilde{K}_{\alpha\beta} \quad (61)$$

where Ψ is the positive conformal factor.

In terms of these new fields the constraint equations read

$$\tilde{D}_\beta \tilde{K}^{\alpha\beta} = -8\pi \tilde{j}^\alpha, \quad (62)$$

$$L_{\tilde{g}}\Psi = -\frac{2\pi\tilde{\mu}}{\Psi^3} - \frac{\tilde{K}_{\alpha\beta}\tilde{K}^{\alpha\beta}}{8\Psi^7}, \quad (63)$$

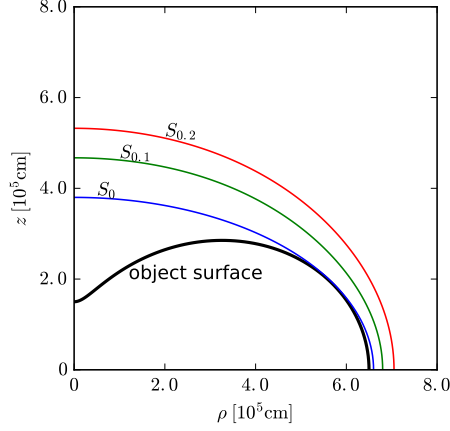


Figure 5: Concave object's surface and short time IMCF evolution of the convex spheroidal surface S_0 enclosing it.

where \tilde{D} is the covariant derivative with respect to \tilde{g} , and we have defined

$$L_{\tilde{g}}\Psi = \Delta_{\tilde{g}}\Psi - \frac{1}{8}\Psi\tilde{R}, \quad (64)$$

$$\tilde{\mu} = \Psi^8\mu, \quad \tilde{j}^\alpha = \Psi^{10}j^\alpha \quad (65)$$

where \tilde{R} is the scalar curvature associated to \tilde{g} .

The momentum constraint (62) can be solved in the following form. Let A_α be a 1-form to be specified and set

$$\tilde{K}_{\alpha\beta} = (\mathcal{L}A)_{\alpha\beta} + \sigma_{\alpha\beta}, \quad (66)$$

where

$$(\mathcal{L}A)_{\alpha\beta} = \tilde{D}_\alpha A_\beta + \tilde{D}_\beta A_\alpha - \tilde{g}_{\alpha\beta} \frac{2}{3} \tilde{D}_\gamma A^\gamma, \quad (67)$$

and $\sigma_{\alpha\beta}$ is an arbitrary trace-free tensor field. Then the momentum constraint has the form

$$\mathbf{L}_{\tilde{g}}A_\alpha = -8\pi\tilde{j}_\alpha - \tilde{D}^\beta\sigma_{\alpha\beta}, \quad (68)$$

where $\mathbf{L}_{\tilde{g}}$ is the elliptic operator

$$\mathbf{L}_{\tilde{g}}A_\alpha = \tilde{D}^\beta(\mathcal{L}A)_{\alpha\beta}. \quad (69)$$

It is important to note that the set of elliptic equations (69) and (63) can be solved on a bounded domain prescribing Dirichlet conditions for Ψ and the analog to Neumann condition for A_α , namely

$$\nu^\alpha(\mathcal{L}A)_{\alpha\beta} = \phi_\beta \quad (70)$$

where ν^α is the outer unit normal to the boundary and ϕ_β is a function on the boundary.

A.1 Conformally flat initial data

Consider a conformally flat initial data, that is

$$\tilde{g}_{\alpha\beta} = \delta_{\alpha\beta} \quad (71)$$

where $\delta_{\alpha\beta}$ is the flat 3-metric. In this case the constraint equations simplify to

$$\partial_\beta \tilde{K}^{\alpha\beta} = -8\pi \tilde{j}^\alpha, \quad (72)$$

$$\Delta \Psi = -\frac{2\pi \tilde{\mu}}{\Psi^3} - \frac{\tilde{K}_{\alpha\beta} \tilde{K}^{\alpha\beta}}{8\Psi^7}. \quad (73)$$

where ∂_α are partial derivatives, Δ is the flat Laplace operator in 3 dimensions and indices are moved with respect to δ .

The solution of equation (72) is constructed as in the previous section. We choose $\sigma_{\alpha\beta} = 0$, hence

$$\tilde{K}_{\alpha\beta} = \partial_\alpha A_\beta + \partial_\beta A_\alpha - \frac{2}{3} \delta_{\alpha\beta} \partial_\gamma A^\gamma, \quad (74)$$

and equation (72) translates into

$$\Delta A^\alpha + \frac{1}{3} \partial^\alpha \partial_\beta A^\beta = -8\pi \tilde{j}^\alpha. \quad (75)$$

Imposing the following condition on the sources

$$\partial_\alpha \tilde{j}^\alpha = 0. \quad (76)$$

we obtain

$$\partial_\alpha A^\alpha = 0, \quad (77)$$

and hence the final set of equation equivalent to (72) are

$$\Delta A^\alpha = -8\pi \tilde{j}^\alpha. \quad (78)$$

The solution of this equation is given by the Green function

$$A^\alpha(x) = 2 \int \frac{\tilde{j}^\alpha(x')}{|x - x'|} d^3 x'. \quad (79)$$

where $|\cdot|$ is the flat norm.

We prescribe $\tilde{\mu}$ to be exactly the border case in the dominant energy condition, namely

$$\tilde{\mu} = \sqrt{\tilde{j}^\alpha \tilde{j}_\alpha}. \quad (80)$$

and therefore the only free data is \tilde{j}_α . We choose this vector to be

$$\tilde{j}^\alpha = a \tilde{\eta}^\alpha, \quad (81)$$

where a is a smooth function of the coordinates and $\tilde{\eta}_\alpha$ is the flat Killing vector. In spherical coordinates (r, θ, φ) , the Killing vector is $\tilde{\eta}^\alpha = \frac{\partial}{\partial \varphi}$ and $a = a(r, \theta)$. Then using (81) we find that the solution to (78) is given by

$$A^\alpha = f(r, \theta) \tilde{\eta}^\alpha, \quad (82)$$

where f satisfies

$$\partial_r^2 f + 4 \frac{\partial_r f}{r} + \frac{\partial_\theta^2 f}{r^2} + \frac{3 \cos \theta \partial_\theta f}{r^2 \sin \theta} = -8\pi a. \quad (83)$$

with the boundary condition

$$\lim_{r \rightarrow \infty} f = 0. \quad (84)$$

It is straightforward to calculate $\tilde{K}_{\alpha\beta}$ from the expression (82), using the Killing equation and the fact that

$$\tilde{\eta}^\alpha \partial_\alpha f = 0, \quad (85)$$

and we obtain the remarkable simple formulae

$$\tilde{K}_{\alpha\beta} = 2\tilde{\eta}_{(\alpha} \partial_{\beta)} f \quad \tilde{K}_{\alpha\beta} \tilde{K}^{\alpha\beta} = 2|\partial f|^2 r^2 \sin^2 \theta. \quad (86)$$

Summarizing, the systems we consider for the numerical computations are prescribed by giving an arbitrary, axially symmetric, function a of compact support. This function describes the location of the matter sources. Given a , the equations (83) with the boundary condition (84) and

$$\Delta \Psi = -\frac{2\pi a r \sin \theta}{\Psi^3} - \frac{|\partial f|^2 r^2 \sin^2 \theta}{4\Psi^7}, \quad \lim_{r \rightarrow \infty} \Psi = 1. \quad (87)$$

Using the sub and super solution method, it can be proven that given a smooth a there exists a unique solution for the non-linear elliptic equation (87).

B Surfaces on conformally flat data

All relevant physical parameters of the initial data and of surfaces on M can be computed in terms of a and Ψ . Let Ω be any domain that contains the matter fields, and let dv_0 , ds_0 be the flat volume and surface element respectively.

The ADM mass is given by

$$m_{ADM} = \int_{\mathbb{R}^3} \left(\frac{|\partial \Psi|^2}{2\pi \Psi^2} + \frac{ar \sin \theta}{\Psi^4} + \frac{2|\partial f|^2 r^2 \sin^2 \theta}{16\pi \Psi^8} \right) dv_0 \quad (88)$$

The angular momentum is

$$J = - \int_{\Omega} ar^2 \sin^2 \theta dv_0. \quad (89)$$

The baryonic mass (as a measure of the quasi-local mass) is given by:

$$M_b = \int_{\Omega} \mu dv = \int_{\Omega} \frac{ar \sin \theta}{\Psi^2} dv_0. \quad (90)$$

Concerning the measures of the size of Ω we calculate the surface area $A(\partial\Omega)$

$$A(\partial\Omega) = \int_{\partial\Omega} \Psi^4 ds_0 \quad (91)$$

and the length of the greatest axisymmetric circle $\mathcal{C}(\partial\Omega)$

$$\mathcal{C} = 2\pi \max_{\partial\Omega} (\sqrt{\eta}) = 2\pi \max_{\partial\Omega} (r \sin \theta \Psi^2). \quad (92)$$

C The IMCF on conformally flat initial data

In this section we derive the evolution equation for the flow surfaces, used in our numerical examples of section 4.

We study the IMCF in $M = \mathbb{R}^3$ with metric $\bar{g}_{\alpha\beta} = \psi^4 \delta_{\alpha\beta}$. It is convenient to introduce a level-set formulation of (6), where the evolving surfaces are given as level-sets of a scalar function u via

$$S_t = \{x^\alpha : u(x^\alpha, t) = 0\}$$

and (6) is replaced by the degenerate elliptic equation:

$$\bar{D}_\alpha \left(\frac{\bar{g}^{\alpha\beta} \partial_\beta u}{|\partial u|_{\bar{g}}} \right) = |\partial u|_{\bar{g}} \quad (93)$$

Note that in our model we can write the mean curvature H of S_t in terms of Ψ :

$$H = \bar{D}_\alpha \left(\frac{\bar{g}^{\alpha\beta} \partial_\beta u}{|\partial u|_{\bar{g}}} \right) = \frac{1}{\Psi^2 |\partial u|} \left(\Delta u + 4 \frac{\partial \Psi \cdot \partial u}{\Psi} - \frac{\partial |\partial u| \cdot \partial u}{|\partial u|} \right) \quad (94)$$

where all the derivatives and dot products are computed with respect to the flat metric.

At this point it is convenient to define an operator \mathcal{P} acting on u :

$$\mathcal{P}u = \Delta u + 4 \frac{\partial \Psi \cdot \partial u}{\Psi} - \frac{\partial |\partial u| \cdot \partial u}{|\partial u|} \quad (95)$$

thus, equation (93) can be written as

$$|\partial u| = \frac{\mathcal{P}u}{\Psi^2 H}. \quad (96)$$

Now, instead of solving this elliptic equation, we will solve an evolution equation for u obtained by taking a total time derivative of u on the surface S_t :

$$\begin{aligned} 0 &= \frac{du}{dt} = \frac{\partial u}{\partial x^\alpha} \frac{\partial x^\alpha}{\partial t} + \frac{\partial u}{\partial t} = \partial_\alpha u \frac{\nu^\alpha}{H} + \frac{\partial u}{\partial t} = \partial_\alpha u \frac{\partial^\alpha u}{\Psi^2 |\partial u|} \frac{1}{H} + \frac{\partial u}{\partial t} \\ &= \frac{|\partial u|}{\Psi^2 H} + \frac{\partial u}{\partial t} = \frac{|\partial u|^2}{\mathcal{P}u} + \frac{\partial u}{\partial t} \end{aligned}$$

where in the second step we have used the IMCF equation, and in the last one we use that H is given by (96), thus we have:

$$\frac{\partial u}{\partial t} = - \frac{|\partial u|^2}{\mathcal{P}u}. \quad (97)$$

We take the surface S_t to be given by

$$u = u(r, \theta, t) = r - v(\theta, t) = 0 \quad (98)$$

and putting this into (97), we arrive at the following evolution equation for v

$$\frac{\partial v}{\partial t} = \frac{1 + \left(\frac{\partial_\theta v}{v} \right)^2}{\hat{\mathcal{P}}v} \quad (99)$$

where we define the operator $\tilde{\mathcal{P}}$ acting on v as

$$\tilde{\mathcal{P}}v = \left(\frac{2}{v} - \frac{\partial_\theta(\sin\theta\partial_\theta v)}{v^2\sin\theta} + \frac{4}{\Psi} \left(\partial_r\Psi|_{r=v} - \frac{\partial_\theta v\partial_\theta\Psi}{v^2} \right) + \frac{\left(\frac{\partial_\theta v}{v}\right)^2(v + \partial_\theta^2 v)}{1 + \left(\frac{\partial_\theta v}{v}\right)^2} \right). \quad (100)$$

Finally, the principal curvatures of S_t are

$$\lambda_\varphi = \frac{2r^2\partial_r\Psi\sin\theta + \Psi r\sin\theta - 2\partial_\theta\Psi\sin\theta u' - \Psi\cos\theta u'}{\Psi^3 r\sin\theta\sqrt{r^2 + u'^2}} \quad (101)$$

$$\lambda_\theta = \frac{r[(r^2 + u'^2)(r^2\partial_r\Psi + r - u''\Psi) + u''u'^2\Psi]}{\Psi^3(r^2 + u'^2)^{5/2}} \quad (102)$$

and S_t is convex if $\lambda_\varphi, \lambda_\theta \geq 0$. Note that in the limit of $\Psi \rightarrow 1$ and $u = \text{const.}$ we obtain the principal curvatures of the round sphere.

$$\lambda_\theta^{\text{sphere}} = \lambda_\varphi^{\text{sphere}} = \frac{1}{r} \quad (103)$$

References

- [1] Andres Acena, Sergio Dain, and Maria E. Gabach Clement. Horizon area–angular momentum inequality for a class of axially symmetric black holes. *Class. Quant. Grav.*, 28:105014, 2011.
- [2] Pablo Anglada. *In preparation*, 2017.
- [3] Pablo Anglada, Sergio Dain, and Omar E. Ortiz. Inequality between size and charge in spherical symmetry. *Phys. Rev.*, D93(4):044055, 2016.
- [4] R. Arnowitt, S. Deser, and C. W. Misner. The dynamics of general relativity. In L. Witten, editor, *Gravitation: An Introduction to Current Research*, pages 227–265. Wiley, New York, 1962.
- [5] Jacob D. Bekenstein. Universal upper bound on the entropy-to-energy ratio for bounded systems. *Phys. Rev. D*, 23:287–298, Jan 1981.
- [6] W. L. Briggs, V. E. Henson, and S. F. McCormick. *A Multigrid Tutorial*. SIAM, Philadelphia, PA, 2nd edition, 2000.
- [7] Maria E. Gabach Clement, Jose Luis Jaramillo, and Martin Reiris. Proof of the area-angular momentum-charge inequality for axisymmetric black holes. *Class. Quant. Grav.*, 30:065017, 2013.
- [8] Maria Eugenia Gabach Clement, Martin Reiris, and Walter Simon. The area-angular momentum inequality for black holes in cosmological spacetimes. *Class. Quant. Grav.*, 32(14):145006, 2015.
- [9] Sergio Dain. Proof of the angular momentum-mass inequality for axisymmetric black holes. *J. Differential Geometry*, 79(1):33–67, 2008.
- [10] Sergio Dain. Inequality between size and angular momentum for bodies. *Phys. Rev. Lett.*, 112:041101, 2014.

- [11] Sergio Dain. Bekenstein bounds and inequalities between size, charge, angular momentum and energy for bodies. *Phys. Rev.*, D92(4):044033, 2015.
- [12] Sergio Dain and Martin Reiris. Area - Angular momentum inequality for axisymmetric black holes. *Phys. Rev. Lett.*, 107:051101, 2011.
- [13] Maria Eugenia Gabach-Clement and Martin Reiris. Shape of rotating black holes. *Phys. Rev.*, D88(4):044031, 2013.
- [14] Gregory J. Galloway and Niall O’Murchadha. Some remarks on the size of bodies and black holes. *Class. Quant. Grav.*, 25:105009, 2008.
- [15] P. Haensel, A.Y. Potekhin, and D.G. Yakovlev. *Neutron Stars 1: Equation of State and Structure*. Astrophysics and Space Science Library. Springer New York, 2007.
- [16] James B. Hartle. Slowly rotating relativistic stars. 1. Equations of structure. *Astrophys. J.*, 150:1005–1029, 1967.
- [17] Jörg Hennig, Carla Cederbaum, and Marcus Ansorg. A universal inequality for axisymmetric and stationary black holes with surrounding matter in the Einstein-Maxwell theory. *Commun. Math. Phys.*, 293:449–467, 2010.
- [18] Shahar Hod. Universal entropy bound for rotating systems. *Phys. Rev. D*, 61:024018, Dec 1999.
- [19] G. Huisken and T. Ilmanen. The inverse mean curvature flow and the Riemannian Penrose inequality. *J. Differential Geometry*, 59:352–437, 2001.
- [20] Gerhard Huisken. Evolution of hypersurfaces by their curvature in riemannian manifolds. *Documenta Mathematica*, pages 349–360, 1998.
- [21] Pong Soo Jang. Note on cosmic censorship. *Phys. Rev.*, D20:834–838, 1979.
- [22] Marcus Khuri and Naqing Xie. Inequalities Between Size, Mass, Angular Momentum, and Charge for Axisymmetric Bodies and the Formation of Trapped Surfaces. arXiv, gr-qc: 1610.04892, 2016.
- [23] Marcus A. Khuri. Existence of Black Holes Due to Concentration of Angular Momentum. *JHEP*, 06:188, 2015.
- [24] Marcus A. Khuri. Inequalities Between Size and Charge for Bodies and the Existence of Black Holes Due to Concentration of Charge. *J. Math. Phys.*, 56(11):112503, 2015.
- [25] Heinz-Otto Kreiss and Omar Eduardo Ortiz. *Introduction to Numerical Methods for Time Dependent Differential Equations*. John Wiley & Sons, Hoboken, NJ, first edition, 2014.
- [26] Edward Malec, Marc Mars, and Walter Simon. On the Penrose inequality for general horizons. *Phys. Rev. Lett.*, 88:121102, 2002.
- [27] Niall Ó Murchadha. How large can a star be? *Phys. Rev. Lett.*, 57(19):2466–2469, 1986.

- [28] Feryal Özel, Dimitrios Psaltis, Ramesh Narayan, and Antonio Santos Villarreal. On the mass distribution and birth masses of neutron stars. *The Astrophysical Journal*, 757(1):55, 2012.
- [29] Martin Reiris. On the shape of bodies in General Relativistic regimes. *Gen. Rel. Grav.*, 46:1777, 2014.
- [30] Richard Schoen and Xin Zhou. Convexity of reduced energy and mass angular momentum inequalities. *Annales Henri Poincaré*, 14:1747–1773, 2013.
- [31] S.-T Schoen R., Yau. The Existence of a Black Hole Due to Condensation of Matter. *Communications in Mathematical Physics*, 90:575–579, 1983.
- [32] Jose M. M. Senovilla. A Reformulation of the Hoop Conjecture. *Europhys. Lett.*, 81:20004, 2008.
- [33] Nikolaos Stergioulas. Rotating Stars in Relativity. *Living Rev. Rel.*, 6:3, 2003.
- [34] László B. Szabados. Quasi-local energy-momentum and angular momentum in GR: A review article. *Living Rev. Relativity*, 7(4), 2004. cited on 8 August 2005.
- [35] W. G. Unruh and Robert M. Wald. Acceleration Radiation and Generalized Second Law of Thermodynamics. *Phys. Rev.*, D25:942–958, 1982.